APPLIED PHYSICS

Acoustofluidic centrifuge for nanoparticle enrichment and separation

Yuyang Gu[1], Chuyi Chen[1], Zhangming Mao[2], Hunter Bachman[1], Ryan Becker[3], Joseph Rufo[1], Zeyu Wang[1], Peiran Zhang[1], John Mai[4], Shujie Yang[1], Jinxin Zhang[1], Shuaiguo Zhao[1], Yingshi Ouyang[5], David T. W. Wong[6], Yoel Sadovsky[5,7], Tony Jun Huang[1]*

Liquid droplets have been studied for decades and have recently experienced renewed attention as a simplified model for numerous fascinating physical phenomena occurring on size scales from the cell nucleus to stellar black holes. Here, we present an acoustofluidic centrifugation technique that leverages an entanglement of acoustic wave actuation and the spin of a fluidic droplet to enable nanoparticle enrichment and separation. By combining acoustic streaming and droplet spinning, rapid (<1 min) nanoparticle concentration and size-based separation are achieved with a resolution sufficient to identify and isolate exosome subpopulations. The underlying physical mechanisms have been characterized both numerically and experimentally, and the ability to process biological samples (including DNA segments and exosome subpopulations) has been successfully demonstrated. Together, this acoustofluidic centrifuge overcomes existing limitations in the manipulation of nanoscale (<100 nm) bioparticles and can be valuable for various applications in the fields of biology, chemistry, engineering, material science, and medicine.

INTRODUCTION

Nanoparticle manipulation is of great importance in various biomedical and biochemical applications, including gene/drug delivery (*1*–*3*), precision bioassays (*4*, *5*), cancer diagnosis (*6*–*8*), and catalyzing reactions (*9*–*11*). Hence, the ability to perform nanoparticle concentration or separation, or achieve self-assembly of nanostructures, has emerged as a prominent interdisciplinary need in many fields. In addition, although there is a strong desire for controlling nanoscale (<100 nm) objects, only a handful of methods can achieve manipulation at this level. Conventional techniques for nanoscale manipulation include ultracentrifugation (*12*), nanopore filtration (*13*), dielectrophoresis (*14*), magnetopheresis (*15*), optical tweezing (*16*), and plasmonic tweezing (*17*). While each of these methods has certain advantages depending on the given application, there are still many drawbacks associated with their routine use. For example, ultracentrifugation and filtration-based manipulation have relatively low sample yields and require long processing periods; optical and plasmonic tweezers provide high precision, but they are usually restricted to manipulating a relatively small number of particles, thus severely limiting their practical applications.

Compared with these methods, acoustofluidics (i.e., the fusion of acoustics and microfluidics)–based techniques have advantages such as high biocompatibility, versatility, and simplistic device design (*18*). The main mechanisms that acoustofluidic methods leverage to control particles are acoustic radiation force and acoustic streaming. Both of these mechanisms can be useful in various applications, especially those involving microparticles (*19*–*24*). However, when dealing with nanoparticles, the fundamental limitation of acoustic-based systems is apparent; namely, there is often an insufficient acoustic radiation force to fully control the nanosized particles (*25*, *26*). One strategy that has been implemented to manipulate nanoscale objects using acoustofluidics is to increase the magnitude of the acoustic radiation force. As previous studies have shown, by increasing the working frequency or by constructing specialized acoustic resonators, the radiation force can be increased by many times, which enables control of submicrometer-sized particles (*27*, *28*). Furthermore, by seeding a fluid with microparticles, the secondary acoustic radiation force, which is increased due to microscale particle interactions, can also be applied to achieve submicrometer-scale control (*29*, *30*). In an attempt to overcome limitations imposed by solely acoustic radiation force–based manipulation of nanoparticles, researchers have also shown a vast improvement in manipulation capabilities by using acoustic controlled streaming motion in combination with acoustic radiation forces (*31*, *32*). Although these aforementioned methods can overcome a certain degree of mismatch between acoustofluidic techniques and nanoscale manipulation, most methods remain focused on submicrometer-scale (>100 nm) manipulation, and limited studies have been performed on acoustic-based manipulation of nanoscale (<100 nm) bioparticles.

Here, we present an acoustofluidic centrifuge system that leverages acoustically driven spinning droplets to manipulate particles with sizes down to a few nanometers. Various functionalities of this system are demonstrated, including nanoparticle concentration, separation, and transport. The basic system is composed of one pair of slanted interdigitated transducers (IDTs) and a circular polydimethylsiloxane (PDMS) containment ring to encapsulate a portion of the droplet and to define its shape. We observed an interesting physical phenomenon where surface acoustic waves (SAWs) can drive droplets to spin along their central axis. This spinning motion initiates Stokes drift along a circular closed path that transfers momentum to the fluid in a manner that notably increases the inner streaming velocity and shear rate within the droplet by 10 to 100 times.

---

[1]Department of Mechanical Engineering and Materials Science, Duke University, NC 27708, USA. [2]Department of Engineering Science and Mechanics, Pennsylvania State University, University Park, PA 16801, USA. [3]Department of Biomedical Engineering, Duke University, NC 27708, USA. [4]Alfred E. Mann Institute for Biomedical Engineering, University of Southern California, Los Angeles, CA 90089, USA. [5]Department of Obstetrics, Gynecology, and Reproductive Sciences, Magee-Womens Research Institute, University of Pittsburgh, Pittsburgh, PA 15213, USA. [6]School of Dentistry and the Departments of Otolaryngology/Head and Neck Surgery and Pathology, University of California, Los Angeles, Los Angeles, CA 90095, USA. [7]School of Medicine, University of Pittsburgh, Pittsburgh, PA 15261, USA.
*Corresponding author. Email: tony.huang@duke.edu

Particles within this "rotational vortex field" follow a helical trajectory and are rapidly concentrated to the center of the droplet as a result of the combination of the acoustic radiation force and drag force. Through numerical simulations and experimental investigations, we demonstrate that acoustic waves can rotate a liquid droplet with a variable sample volume (from nanoliters to microliters), to influence nanoparticles of various sizes (from a few nanometers to a few micrometers). As a result, leveraging droplet resonance enables 28-nm nanoparticles, as well as strands of DNA, to be concentrated within 1 min. In addition, by building an acoustofluidic centrifuge system with dual rotating droplets, we can separate nanoparticles of various sizes, including exosome subpopulations, with high purity. To the best of our knowledge, this work marks that an acoustic-based technique can achieve isolation of different exosome subpopulations. The comprehensive theoretical modeling and matching experimental results performed using this new acoustic-mediated nanoparticle manipulation platform can be extrapolated to applications in simplifying transfection, automating vesicle cargo loading, and accelerating liquid biopsies.

RESULTS

Working mechanism of the acoustofluidic centrifuge

As shown in Fig. 1, the basic experimental configuration of the acoustofluidic centrifuge includes one pair of slanted IDTs with a PDMS ring aligned in the middle. The slanted IDTs enable broadband frequency excitation because of the varied finger spacing across the widths of the transducers. The PDMS ring confines the boundary of the fluid such that when a water droplet is added to the container, it forms its equilibrium hemispherical shape when gravity and surface tension forces are balanced. When an electrical signal is applied to the slanted IDTs, two traveling SAWs propagate along the substrate from two opposing directions and enter the two flanks of the droplet. The droplet spinning will experience three regimes from its nonspinning to stable spinning mode. (i) With a small acoustic amplitude excitation, internal vortex streaming can be generated, while the droplet will remain in its equilibrium shape due to insufficient acoustic radiation pressure acting on the interface and the intensity of acoustic streaming. (ii) As the acoustic amplitude increases, the length of the acoustic wave propagation before being fully attenuated becomes longer, and the vortex streaming is enhanced as well. These effects will tend to break the equilibrium of the liquid-air interface while the droplet's bottom and side boundaries remain constrained within the PDMS ring, resulting in slight oscillations of the fluid surface. (iii) As momentum accumulates and the surface tension of the droplet attempts to remain in balance with the acoustic radiation pressure and centrifugal force, the droplet gradually deforms into a concave ellipsoid shape and reaches a stable spin mode with a periodic rotational boundary deformation, which forms a "rotational capillary wave" propagating along the free surface of the droplet. In this mode, particles within the droplet migrate toward the center of the droplet following a dual-axis rotational trajectory. One axis is with respect to the droplet, and the other axis is with respect to the particle. This dual-axis particle trajectory follows a helical path with the particle itself also rotating (as shown in the dashed box of Fig. 1A and indicated by the green arrow).

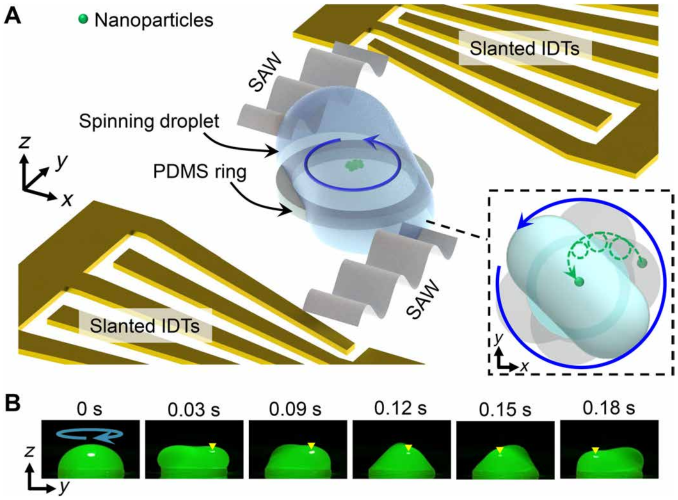

Fig. 1. Operating mechanism of the acoustofluidic centrifuge platform. (**A**) Illustration of the acoustofluidic centrifuge system. The droplet is placed on a PDMS ring that confines the fluid boundary and is located between two slanted IDTs. As the SAWs propagate into the droplet, the liquid-air interface is deformed by the acoustic radiation pressure, and the droplet starts to spin. Particles inside the droplet will follow helical trajectories (inset) under the influence of both induced vortex streaming and the spinning droplet. (**B**) A sequence of images showing the side view of a 30-μl rotating droplet. The SAW is activated at 0 s. The sequence shows that as the droplet starts spinning, it stretches out to a concave ellipsoid shape, as illustrated in (A). Yellow arrow indicates the reference position that rotates along with the spinning droplet.

As indicated in Fig. 1B, compared with the original spherical cap shape, the spinning droplet has a lower height but a higher maximum equatorial radius due to stretching in the horizontal direction. From the top view, as shown in Fig. 2A, the equilibrium cross section of the droplet is a spinning, two-lobed, elliptical shape. The green line a-a′ (Fig. 2, A and B) indicates the droplet radial distance at a fixed location over time. To accurately measure the rotational speed of the spinning droplet, the change in this radial distance is plotted as a waveform (Fig. 2C) via image processing of the image in Fig. 2B. The rotational speed of the spinning droplet can then be calculated via a Fourier transform of this waveform. The peaks of the waveform correspond to twice the rotational frequency since the dual lobes of the single droplet will cross the detection line two times each cycle. Extracting the droplet speed from the waveform, we can then compare the spin rate to classical droplet oscillation dynamics (*33*, *34*)

$$\omega_n{}^2 = n(n+1)(n-1)(n+2)\frac{\sigma}{r^3[(n+1)\rho_{\text{liquid}}+n\rho_{\text{air}}]} \qquad (1)$$

where n is the spherical harmonic degree that corresponds to the lobe number during spin, r is the droplet's radius (e.g., the radius of the spherical cap), σ is the surface tension, and ρ_{liquid} and ρ_{air} are the density of the liquid and air, respectively. This oscillation equation calculates the free oscillation frequency of a spherical droplet whose lobes repeatedly stretch and contract without spinning (*35*), as opposed to the continuous rotational deformation observed in our platform. The radius of the droplet can be calculated from the volume of the droplet; a pipette is used to generate a droplet with the known volume of V, and given that the PDMS ring has a radius of a and a height of h (as depicted in Fig. 2D), the radius of the droplet is calculated using the following relationship

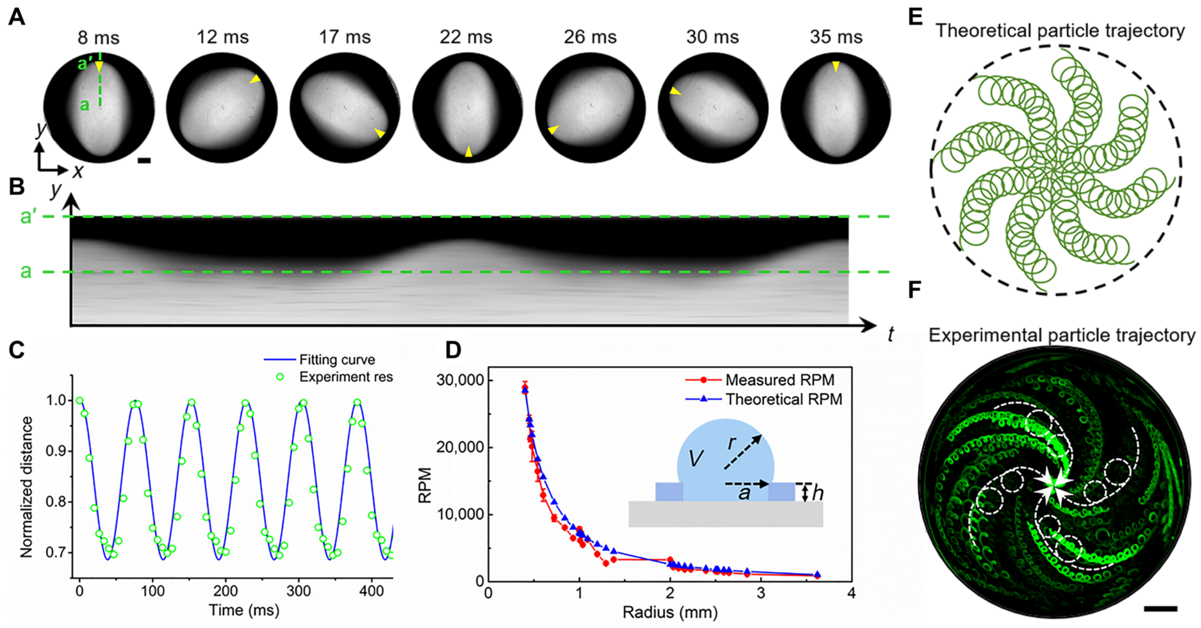

Fig. 2. Characterization of droplet spin and particle movement in the acoustofluidic centrifuge device. (**A**) A sequence of images showing the top view of a spinning droplet under a microscope. (**B**) Corresponding time sequence of stacked images along the line a-a′, which shows the periodic spin of the ellipsoid droplet. (**C**) The instantaneous velocity at a point on the spinning droplet can be extracted from this normalized fit of the distance change versus time (B). (**D**) Theoretical and experimental droplet rotation speed [rotations per minute (RPM)] versus the change in droplet radius. The volume (*V*) of the droplet refers to the volume above the PDMS ring. (**E**) Theoretically calculated and (**F**) experimentally observed particle trajectories showing the dual rotation modes; particles trace a helical path as they approach the center of the droplet while also rotating around their local axes. Scale bar, 500 μm.

$$V-\pi a^2 h=\frac{\pi}{3}\left(r+\sqrt{r^2-a^2}\right)^2\left[3r-\left(r+\sqrt{r^2-a^2}\right)\right] \qquad (2)$$

For example, for a PDMS ring with a radius of 1.00 mm and a height of 0.55 mm, a 10.0-μl droplet has a radius of ~1.29 mm. The results shown in Fig. 2D indicate that there is a consistent correlation between the measured spin speed and the oscillation speed calculated using Eq. 1. Thus, the spinning droplet and the standard oscillatory motion are similar, where the droplet is forced from its equilibrium state in both cases. In our experiment, droplets with volumes from 60 nl to 90 μl were tested. This corresponds to droplet radii from 0.3 to 3.6 mm.

We also studied whether parameters related to the acoustic field influence the spin motion (figs. S1 to S3). First, we used different acoustic frequencies (7.5 to 11 MHz) to drive the spin of a 30-μl droplet (fig. S1). Results showed that the spin can be excited over a wide range of frequencies as long as the acoustic wave enters the droplet from a position that has a slight bias from its center line. We also found that frequency changes will not cause a major change to the spin speed. This observation is understandable since the rotational speed is primarily determined by the properties of the droplet instead of the external excitation (as per Eq. 1). On the other hand, as the applied power is increased, the droplet will initially maintain its equilibrium shape and then start to experience small oscillations until the acoustic power reaches a threshold value. At this threshold, the droplet enters its stable spinning mode, and the updated equilibrium shape (e.g., a concave ellipsoid shape) will be further stretched with increased power, while the spin rate will not be affected. Notably, with higher droplet volumes, higher-order spin modes are observed when the droplet begins to spin, with four- or six-lobed droplets that form during rotation. As shown in fig. S3 (C and D), four- and six-lobed shapes are visible when dealing with droplets with volumes of 50 and 80 μl, respectively. However, as their momentum increased, both of the higher-order modes reverted to two-lobed shapes. The outline of the four spin modes ($l = 1, 2, 4, 6$) shown in fig. S3 fit the theoretical model given by (*35*)

$$r(\varphi,t)=a\left[1+\varepsilon_l(t)\cos(l\varphi+\varphi_0)\right] \qquad (3)$$

where $\varepsilon_l(t)=\varepsilon_0\cos(\omega_l t)$, and a is the equatorial radius of the droplet at its initial equilibrium state, $\varepsilon_l(t)$ and ε_0 are the transient deviation amplitude and its oscillation amplitude, respectively.

Next, we focused on analyzing the motion of particles within the spinning droplet. Many previous studies have shown that SAWs can induce acoustic streaming vortices inside a droplet (*26*, *36*, *37*). It is also well known that particles are subject to both a drag force, which arises from acoustic streaming, and an acoustic radiation force. However, the current literature largely focuses on microparticles within a droplet that has a static shape (*26*, *36*, *38*). Within a spinning droplet, unlike the curvilinear particle path in a traditional SAW-driven droplet, we observed that particles not only move along the vortex-shaped streamline but are also influenced by the angular momentum of the continuously rotating droplet. Experimentally, we found that particles move along helical trajectories that correspond to a Stokes drift effect, while the localized spinning motion causes the water wave at the liquid-air interface to propagate along a circular path and results in a rotating Stokes drift. As shown in Fig. 2 (E and F), by monitoring the movement of 1-μm particles using a fast camera and by analyzing the videos using particle tracking velocimetry, we can observe the helical-shaped trajectory that the particles follow. It can be seen that the particles generally travel along a larger vortex path, with multiple smaller circular movements along the path to the droplet center; notably, the frequency of the smaller-scale circular motion appears to be equal to the frequency of the bulk droplet spin, meaning that the particle makes one local rotation while simultaneously moving closer to the droplet's global center along its helical path during each rotation of the droplet.

After quantifying the particle velocity inside the droplet, we found that the droplet spin and the resulting localized rotation trajectory have a more substantial effect than simply modifying the trajectory of the particles as they travel toward the droplet's center. We first qualitatively investigated particle motion by dispersing 10-μm polystyrene (PS) particles inside a 20-μl droplet, which corresponds to a droplet radius of 2.39 mm and spin speed of 2741 ± 24 rpm. We found that the particles became concentrated in 0.12 s, which is ~10 to 100 times faster than previously reported acoustic concentration devices (*26*, *39*). We then measured the velocities of 1-μm PS particles within the droplet using digital particle image velocimetry (*40*, *41*). As shown in Fig. 3C, initially the droplet struggles to spin under a 15-Vpp (peak-to-peak voltage) excitation and yields a particle velocity of ~15 mm/s. However, as the input power is increased, the acoustic streaming becomes stronger, and the droplet starts to spin. We observed that the particle velocity increased notably with an 18-Vpp excitation signal, which corresponds to the voltage that causes the droplet to fully enter its spin mode. When the input voltage reaches ~40 Vpp, the average particle velocity can reach nearly ~100 mm/s. To identify the effects of droplet spin, a numerical simulation was performed at the same input power without the droplet spinning (e.g., the droplet remains in its equilibrium hemispherical state) and compared with the velocity within a spinning droplet. At low power levels, the particle velocities between the experiment and simulation had a very small difference. However, the velocity difference became larger, with as much as ~80 mm/s variance once a higher power was applied. Moreover, we performed a numerical simulation to calculate the shear rate inside the droplet under different spin speeds, as shown in Fig. 3D. We found that the shear rate inside the spinning droplet had increased and was positively correlated with the spin speed. Compared with a nonspinning droplet in which the shear rate was only generated by vortex acoustic streaming, the shear rate of a spinning droplet increased several times over as the rotational rate increased. We also noted that, unlike the normal acoustic streaming–induced shear rate distribution, which usually decreases rapidly away from the boundary, the shear rates within the spinning droplet remain high near the droplet center. This could potentially explain the rapid concentration of the microparticles since the droplet spinning enhanced both vortex streaming velocity and the fluid deformation within the droplet. While the entire fluid domain is shown as spinning, the essence of this spinning motion is the boundary periodic deformation along the radial axis. This continuous boundary deformation can generate a secondary flow along the radial direction, which can push the particles into the inner orbit of the vortex streaming and further propel the particles toward the center. Although the particle displacement has a small oscillation along the radial direction due to the continuous stretching and compressing of the droplet, the overall impact is to push the particles inward (fig. S4). Thus, as this inward pushing effect accumulates, nanoparticles can be concentrated to the droplet center. To validate this hypothesis, we also developed a numerical simulation for this continuous deformation–induced secondary flow and concentration phenomenon (fig. S4).

Differential concentration of nanoparticles via acoustofluidic centrifuge

For particles with diameters smaller than 1 μm in a droplet, the drag force generated by both acoustic streaming (tangential direction) and spinning-enhanced secondary flow (radial direction) plays a notable role in driving the particles to move along the fluid

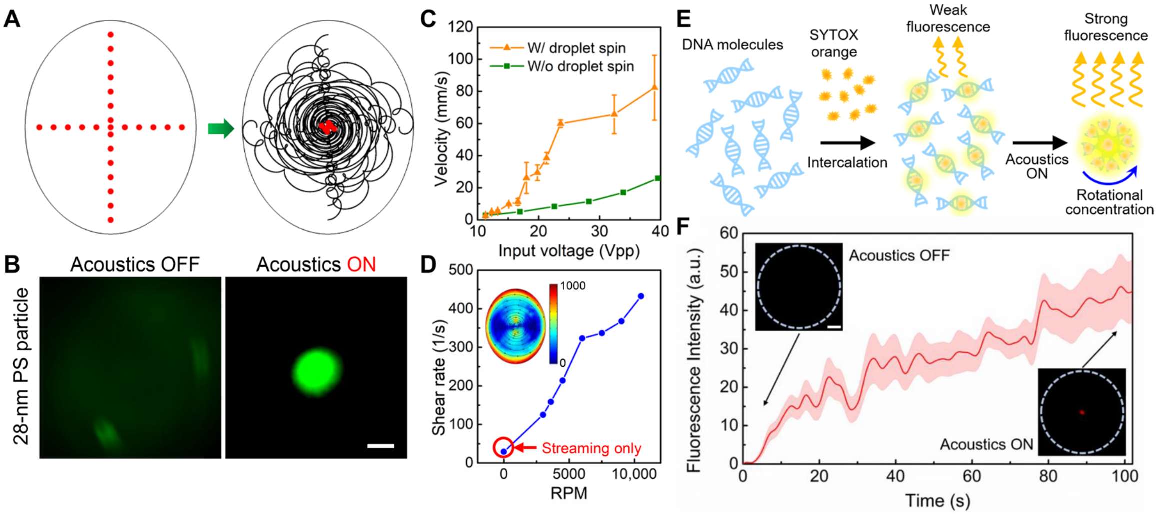

Fig. 3. Rapid nanoparticle enrichment via acoustofluidic centrifuge. (**A**) Numerically simulated particle trajectory within a spinning droplet. As the droplet starts to spin, the particles that were initially randomly distributed inside the droplet (left) follow a helical trajectory until concentrated at the middle of the droplet (right). (**B**) Fluorescence images before (left) and after (right) the acoustic field is turned on, which shows the enrichment of 28-nm PS particles. Scale bar, 50 μm. (**C**) Streaming velocity with (experimental result) and without (simulation result) droplet spinning. (**D**) Plot of the calculated average shear rate inside the droplet versus speed. The shear rate increases with a higher spinning speed and rises to several times higher than the shear rate when there is no rotating droplet (streaming only). (**E**) Flowchart showing the process of DNA enrichment and fluorescent signal enhancement in a spinning droplet. (**F**) Plot of the measured DNA fluorescence intensity versus time in the spinning droplet. Insets: Fluorescence images before and after signal enhancement. Scale bar, 50 μm. a.u., arbitrary units.

streamlines (see fig. S5 and table S1 for the involved factors and forces characterization). As indicated in previous studies (*36*, *39*), the particle trajectory and end position in a sessile droplet are mainly related to two factors: (i) the ratio between the attenuation length of the acoustic wave ($L_s = \rho_s c_s \lambda_s / \rho_f c_f$) and the droplet radius (r_d), where ρ_s, ρ_f, c_s, c_f, and λ_s are the density, acoustic velocity of the substrate and fluid, and the wavelength of the SAW in the substrate, respectively; (ii) the ratio between the particle size and the acoustic wavelength in the fluid ($\kappa = k_f a_p$), where k_f is the wave number in the fluid and a_p is the radius of the particle. When the wave attenuation length is larger than the droplet radius ($L_s > r_d$), and the particle size is small compared with the wavelength in the fluid ($\kappa < 1$), particles inside the vortex streaming field will move and concentrate to the center. When dealing with nanoparticles, the aforementioned secondary flow induced by spinning motion will have a drag force component in the radial direction and dominate the concentration that can gradually bring the particles inward. We then numerically and experimentally proved that nanoparticles can be rapidly (within ~1 min) concentrated in the spinning droplet, with particle sizes down to 28 nm in diameter, as shown in Fig. 3 (A and B).

Rapid concentration of nanoparticles can enable various applications such as fluorescence-based biospecimen detection. For instance, we can detect DNA molecules in our acoustofluidic centrifuge system with a fluorescent dye called SYTOX that enhances its fluorescence more than 500-fold upon intercalation with the DNA. As shown in Fig. 3 (E and F), by mixing DNA strands with this fluorescent marker, this method can substantially enhance the fluorescent signal and detect the tagged DNA within a relatively short period (~100 s). Figure 3E provides a flowchart of the experimental procedure, where SYTOX orange dye is added into the sample droplet that contains the DNA molecules. After intercalation, the DNA will start to express a fluorescent signal. However, without concentration, the fluorescent signal is too weak to be detected (Fig. 3F). In contrast, when the acoustic signal is generated and droplet spin is started, the DNA is concentrated and the signal is amplified (Fig. 3F). To assess the ability to avoid false positives, we noted that while only using the SYTOX dye (without DNA molecules) in the spinning droplet, there was no enhanced fluorescence observed. This proves the capability of our acoustofluidic centrifuge for DNA concentration.

In addition to the rapid enrichment of nanoparticles, we also showed that the system is capable of differentially concentrating nanoparticles of varying sizes. The interplay of the acoustic parameters (e.g., frequency and amplitude) and the droplet dimensions generates different particle trajectories for different-sized particles within the same droplet. As the combined radial force continuously pushes the particles toward the droplet center, different particles share the same final equilibrium position (center region), while the time scale and migration speed for reaching this position are different. Specifically, when nanoparticles with two different sizes are contained within a spinning droplet, the larger particles will experience higher acoustic radiation forces and drag forces and smaller effects from Brownian motion. Numerical simulations were conducted to show that nanoparticles can be differentially concentrated with a small size difference (e.g., the separation of 28- and 100-nm-diameter particles) as shown in Fig. 4A. Experimental results verified this effect, as the 100-nm PS particles were concentrated to the center of the droplet, while the 28-nm PS particles remained randomly dispersed throughout the droplet (see Fig. 4, B to D). Here, a 10-μl droplet (r = 1.29 m, RPM = 3313 ± 35) was used with an input acoustic frequency of 21.7 MHz and a power of 32.4 Vpp.

Dual-droplet acoustofluidic centrifuge

Although nanoparticles of different sizes can be differentially concentrated within a single droplet by concentrating the larger particles to the middle, this single-droplet acoustofluidic centrifuge device has a major flaw: In this single-droplet device, differential concentration and retrieval of the subsets of nanoparticles are conducted within the same droplet, which unavoidably affects the purity of the target nanoparticles with distinctive sizes. To address this concern, we developed a dual droplet–based acoustofluidic centrifuge device that is practical for nanoparticle separation applications. The acoustofluidic centrifuge device has two individual spinning droplet units connected by a microchannel to provide a particle passage. As shown in Fig. 5, by exciting two pairs of SAWs propagating asymmetrically across the flanks of the droplets, both of the droplets will spin simultaneously. Two acoustic beams can be generated with a single IDT by using a frequency shift keying to switch between two different excitation frequencies and excitation locations along the width of the IDT (see fig. S7 for configuration details).

For this demonstration, two droplets with different volumes are used (4.0 and 5.0 μl), which correspond to average rotational speeds of 6867 ± 160 and 5674 ± 98 rpm, respectively. Different-sized

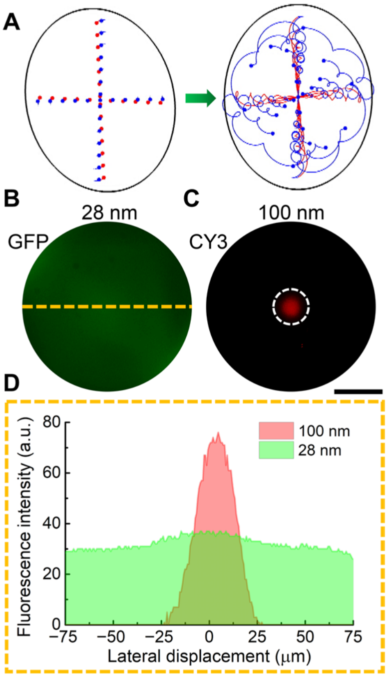

Fig. 4. Differential nanoparticle concentration via acoustofluidic centrifuge. (**A**) Numerical simulation results showing the difference in nanoparticle trajectories for particles with sizes of 100 nm (red) and 28 nm (blue). While the 100-nm particles become concentrated in the center of the spinning droplet, the 28-nm particles follow a helical trajectory but remain randomly distributed throughout the droplet. GFP, green fluorescent protein. (**B**, **C**) Microscope images showing the experimental result of particle separation with 100- (C) and 28-nm (B) particles. Scale bar, 100 μm. (**D**) Fluorescence intensity along the axis of the droplet showing the concentration effect on the 100-nm particles.

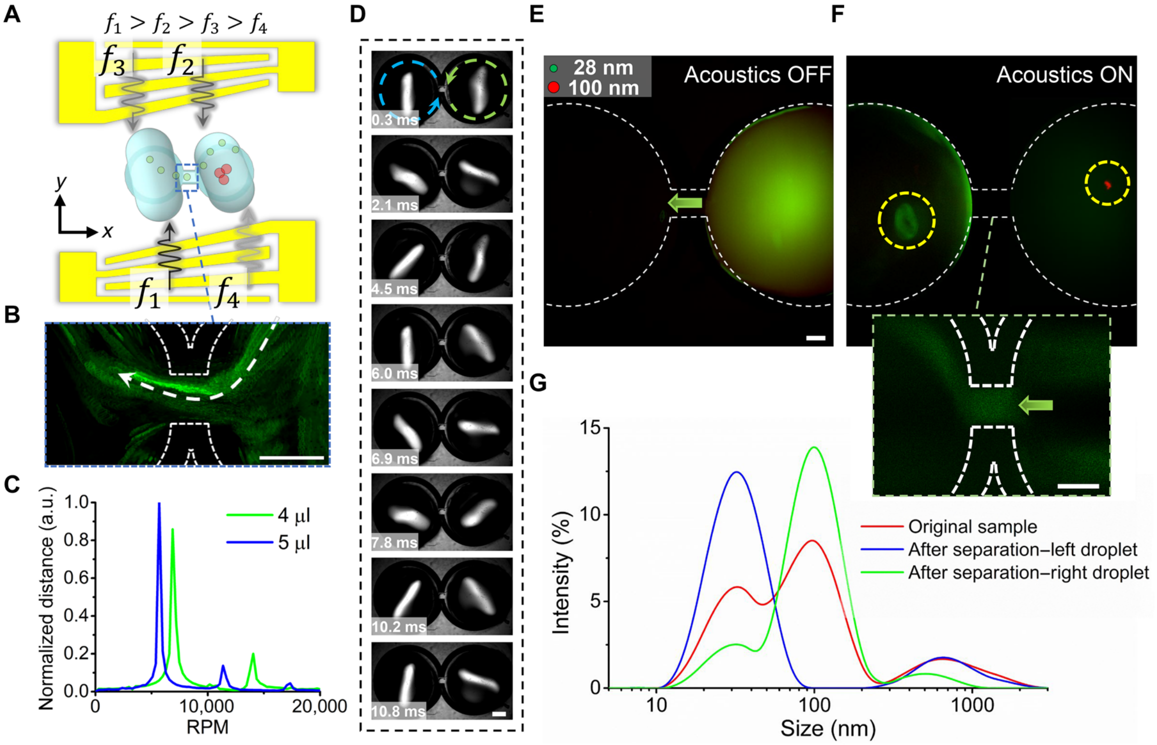

Fig. 5. Particle separation and transport via a dual-droplet acoustofluidic centrifuge. (**A**) Schematic of the dual-droplet acoustofluidic centrifuge. This dual-droplet functionality is achieved using binary frequency shift keying, which involves sequentially shifting between two frequencies for each IDT. With a high shifting frequency, two droplets can be rotated simultaneously. The two droplets are connected by a microchannel, which serves as the passage for particle transport. Here, the specific frequencies are 15.3 MHz (f_4), 15.7 MHz (f_3), 20.3 MHz (f_2), and 21.7 MHz (f_1), with a shifting frequency of 100 kHz. (**B**) A composite image showing the particle trajectory through the center channel. (**C**) The Fourier transform of the waveform plot of a fixed point on the droplet as it spins, indicating the peak rotational frequency of the two droplets with different volumes. (**D**) Image sequence showing the top view of dual-droplet acoustofluidic centrifuge. Fluorescence images (**E**) before and (**F**) after the acoustic signal is turned on, showing the nanoparticle separation and transport from one droplet to another. Inset: Fluorescence image of the middle channel indicating the particle transport process. (**G**) Particle size distribution comparison between the pre- and postseparation samples. The original sample, which was placed into the right droplet, has two peaks at 28 and 100 nm. After separation, most of the 28-nm particles have been separated and have been transported to the left droplet, which has only one peak at 28 nm. Scale bars, 200 µm.

particles were initially seeded into the right droplet, while initially the left droplet did not have any particles (Fig. 5E and fig. S9A). After the acoustic waves were turned on, particles were separated within the right droplet with the larger particles concentrating to the center and the smaller particles remaining dispersed within the right droplet. However, since the spinning velocity of the two droplets is different, there is a deformation speed difference between the two domains. Hence, there is an extra spinning–induced radial drag force from the high–spin velocity region toward the low-velocity region, in addition to convective flow, generated within the fluidic channel between the droplets (fig. S8). This mechanism allows for the smaller particles, which are dispersed within the right droplet, to be transferred into the left droplet. In addition, the acoustic radiation force near the entrance of the right droplet also forces particles into the microchannel toward the left droplet. Experimentally, it was observed that the acoustic beam (f_2 and f_4) accelerates the particles and pushes the particles into the microchannel. At the same time, the acoustic beam (f_1 and f_3), which has a higher frequency and a propagation path closer to the center of the left droplet, further accelerates the particles exiting from the channel. After the smaller particles enter the left droplet, they are, to a certain degree, further concentrated (Fig. 5F and fig. S9, B and C) into the middle of the droplet. This is in contrast to the phenomenon observed in the right (single) droplet, where the 28-nm-diameter particles remained dispersed as the 100-nm-diameter particles are concentrated (as shown in Fig. 4B and C). This may reflect the fact that the concentrated larger particles reduce the size of the streaming vortex, which will prevent the concentration of smaller particles, as also observed in a previous study (*26*).

After separating the two different-sized particle distributions using this dual-droplet system, we characterized the separation and transport performance by measuring the particle size distribution in both droplets using a Zetasizer. As shown in Fig. 5G, most of the remaining particles within the left droplet (blue line) had diameters less than 100 nm. This indicates that after the separation, the left droplet contains mostly 28-nm particles, whereas most of the particles in the right droplet were 100-nm particles. It is worth noting that, on the basis of our experimental observation and characterization, to achieve high separation yield and purity, the two types of particles would need to have a diameter ratio higher than 1.5, as the force difference would be large enough to achieve separation instead of simultaneous concentration in one droplet.

We also used this dual droplet–based acoustofluidic centrifuge system to perform exosome subpopulation separation. Exosomes are nanoscale extracellular vesicles (30 to 150 nm) that carry molecular cargo from their cell of origin. They have emerged as a potentially powerful vector for biomedical research, biomarker discovery, disease diagnostics, and health monitoring (*42*, *43*). It has been reported that exosomes have three distinct subpopulations (i.e., large exosomes, 90 to 150 nm; small exosomes, 60 to 80 nm; and exomeres, ~35 nm), which exhibit different physical and biological properties (*44*–*46*). Among these three subpopulations, exomeres, a nonmembranous nanoparticle, have the smallest size and distinctive cargos compared with the other two subpopulations. While the recent discovery of exosome subpopulations has excited researchers because of their potential to revolutionize the field of noninvasive diagnostics, exosome subpopulations have yet to be used in clinical assays; this is largely due to the difficulties associated with separation of the nanosized exosome subpopulations. Since our dual-droplet acoustofluidic centrifuge system can concentrate and separate nanoparticles with a fine size difference, we have used it to perform exosome subpopulation separation. We initially placed the exosome sample into the right droplet and began the experiment with pure phosphate-buffered saline (PBS) in the left droplet. The nanoparticle size distribution from the original sample and that within the right droplet after separation were extracted using the pipettes (see fig. S10 for schematic of sample extraction) and measured using a nanoparticle tracking analysis (NTA) system. As shown in Fig. 6 (A to C), in the original sample, there are multiple peaks within the size range of the exosome subpopulations beneath the 150-nm size range. After the separation and transport process, there are two major size distribution peaks that remain in the right droplet. Meanwhile, in the left droplet, most of the particles measure below 50 nm. The structures within the three different samples (original, right droplet after separation, and left droplet after separation) were transmission electron microscopy (TEM) imaged (Fig. 6, D to F, left), which supported the results of the NTA measurements. Figure 6 (D to F, right) provides exosome counts from the TEM images and shows a larger percentage of exomeres in the left droplet, again supporting the NTA measurements. These results demonstrate that this dual-droplet acoustofluidic centrifuge system can be used to rapidly fractionalize exosome samples into different subpopulations. It is worth noting that the peaks of the particle size distribution from the NTA measurement have small shifts before and after separation. This phenomenon may be due to the blocking effect of the intense light scattering of large particles as the size of the particle distributions are different in the pre- and postseparation sample. This insufficient polydisperse sample resolution, although difficult to avoid, may be reduced by minimizing the large nanoparticle effect from particles with size ranges out of the realm of interest (see fig. S11).

DISCUSSION

Our acoustofluidic centrifuge uses SAWs to push a droplet out of its equilibrium shape and forces it to spin on its center vertical axis when the fluid boundary is partially confined. This rotational velocity is independent of the acoustic parameters but closely related to the radius of the droplet. This allows the spin rate to be tuned by either changing the volume of the droplet or the size of the PDMS confinement ring. Meanwhile, this spin motion can also be extended to different organic liquids (fig. S12) that are often used for cell/nanoparticle handling (e.g., PBS, cell culture medium, or bovine serum albumin). In a spinning droplet, Stokes drift rotates and forms a closed path, creating a helical trajectory that particles inside the droplet will follow toward the droplet center. This effect is similar to the observations in a recent study into liquid-interface metamaterials (*47*), where the Stokes drift serves as a pathway for wave momentum to be transferred into the fluid and influence particle motion. Although this analogy between the two different systems is remarkable, the difference is stark as well. With the acoustofluidic centrifuge system, high-frequency acoustic waves will propagate into the fluid and generate acoustic streaming and acoustic radiation forces, which both act on the particles and push the particles toward the center of the droplet, as opposed to along specific orbits. The spinning of the droplet not only enables the helical trajectory but also increases the speed of particle concentration by a factor of ~10^2 to 10^3 times by substantially enhancing the streaming velocity along with the secondary flow–induced radial drag force for nanoparticles. All of these phenomena form an interesting and functional system that bridges the gap between acoustofluidics and nanoscale bioparticle manipulation.

On the basis of experiments and numerical simulations, we have shown that particles with sizes ranging from several nanometers (i.e., DNA molecules) to micrometers can be rapidly concentrated in our acoustofluidic centrifuge system. Furthermore, a practical method to separate nanoparticles with different size distributions was demonstrated using a dual-droplet acoustofluidic centrifuge system. This dual-droplet system could be further expanded to a multistage nanoparticle separation or enrichment system in which multiple (>2) groups of nanoparticles can be separated into different outlets in one device. Many bioparticles have sizes that range in the nanoscale or submicrometer scale (e.g., DNA, exosomes, bacteria, proteins, or viruses), and the enrichment and separation of these bioparticles are of great importance in biology, chemistry, and medicine. However, the current methods for nanoparticle enrichment and separation, such as ultracentrifugation, often require a large sample volume (typically >10 ml) and a long processing time (several hours to several days) with relatively low yield (5 to 50%) and purity (23 to 70%) (*48*, *49*). By combining acoustic waves and fluid motion, this acoustofluidic centrifuge has advantages in both of these regards. This device can flexibly handle smaller sample volumes ranging from nanoliters to microliters, and processing times (1 min or less) are much shorter than currently available nanoparticle concentration/separation mechanisms while a relatively high yield and purity (>80%) can be sustained (see table S3 for the comparison of different nanoparticle/exosome separation techniques). Furthermore, it is an open microfluidic device with a simple fabrication process. This allows for easy accessibility to the droplet via a pipette, eliminating the need for external pumps, valves, or other flow control devices (*50*). However, some remaining issues of our method should also be noted that can be improved with future study. One is a low sample volume (below 20 μl) that can be processed at one time; this low sample volume is a result of needing to have a strong enough spinning speed and internal streaming velocity. Meanwhile, as an open microfluidic design, it will still suffer from potential evaporation problems if a long processing time is required. These issues might potentially be improved by optimization of device parameters or temperature and moisture control with future development.

The effects of different factors involved in the operation of this acoustofluidic centrifuge have been explored in our study to better understand and improve the device performance. For example, if the streaming within the droplet is too strong, then it may induce

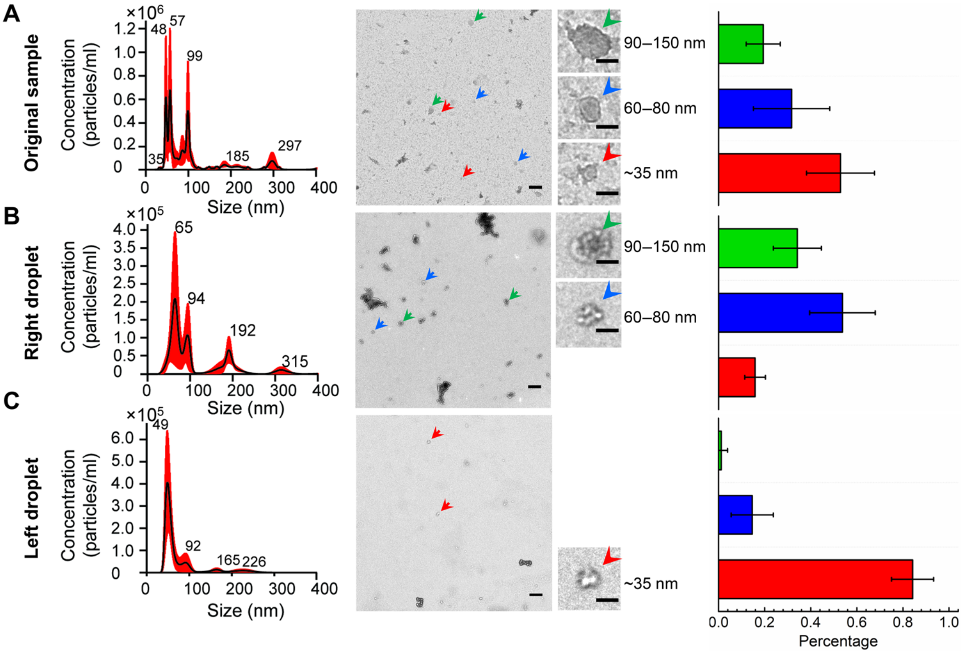

Fig. 6. Exosome subpopulation separation and transport in an acoustofluidic centrifuge. (**A**) The particle size distribution (left) of the original sample analyzed using NTA. The corresponding transmission electron microscopy (TEM) image (middle) is taken from each respective sample. Insets: Magnified images of the exosome sample with different sizes, with plots providing the total particle size distribution as measured in each TEM image. (**B**) The particle size distribution of the sample in the right droplet after the separation and transport process, and corresponding TEM images and plots. (**C**) Particle size distribution of the sample in the left droplet. Particles with a diameter less than 50 nm are transported from the right droplet to the left. The corresponding TEM image and plots are also provided. Scale bars, 200 nm (TEM image) and 50 nm (insets). Each set of the NTA data was obtained from at least three NTA assays. The black line and the red area represent the fitting curve and the error bar, respectively. For each individual sample used for NTA measurement, five subsamples are collected and combined to provide sufficient particle numbers for measurement. Each counted particle percentage plot is averaged from TEM images from five individual trials (see table S2 for detailed count and percentage for each sample).

the redispersion of concentrated particles, especially in smaller droplets that have a high rotational velocity. On the other hand, if the streaming is too weak, then it may cause insufficient enrichment. Thus, device-operating parameters must be optimized for particular applications. In our acoustofluidic centrifuge, many factors need to be considered for optimizing nanoparticle motion within the rotational vortex (e.g., Brownian motion, the extra shear rate, and the secondary flow drag force in the spinning droplet). In this regard, we performed numerical simulations to investigate the interaction between these factors. This simulation model is presented as an efficient tool to estimate the proper streaming velocity and radial force that is needed to concentrate/separate nanoparticles with different size distributions, and the trajectories of different-sized particles could be simulated and traced as well. Moreover, the numerical simulation was used to isolate the effects of droplet spinning motion from acoustic streaming (fig. S13), which is difficult to observe during experimentation because the particle motion within the droplet is an intertwined effect combining these two motions. Increasing our understanding of how these forces individually affect the particle motions within the droplet could lead to a more efficient acoustofluidic centrifuge system in the future.

In summary, we demonstrated an acoustofluidic centrifuge platform that can efficiently and rapidly enrich or separate nanoscale bioparticles. We believe that this platform can substantially simplify and speed up sample processing, detection, and reagent reactions in various applications such as point-of-care diagnostics, bioassays, and liquid biopsies.

MATERIALS AND METHODS

Device design, fabrication, and operation

The slanted IDTs (5-nm Cr and 50-nm Au) were fabricated on a 128° Y-cut lithium niobite ($LiNbO_3$) wafer (Precision Micro-Optics, USA) using standard photo-lithography followed by electron beam evaporation and a lift-off process. Silver epoxy (MG Chemicals, USA) was used to connect wires to the IDT electrodes. The microchannels were fabricated by standard soft lithography and a mold-replica procedure. The PDMS rings were cut to the desired size from a 0.55-mm-thick PDMS film using punches (Robbins Instruments, USA). The PDMS parts and $LiNbO_3$ substrate were bonded together after 3 min of treatment in an oxygen plasma cleaner (Harrick Plasma, USA). Three slanted IDT configurations used in our setup corresponding to different droplet volume ranges (~10 μl, ~1 μl, and ~100 nl). The first has an electrode finger width and spacing gap that decrease linearly from 140 to 70 μm, corresponding to SAW frequencies from 7 to 14 MHz. The second has finger widths from 75 to 35 μm, corresponding to 13 to 28 MHz. The third has widths from 32.5 to 17.5 μm, corresponding to 30 to 56 MHz. Two function generators (DG 3012C, Teletronics Technology Corporation, USA) and two amplifiers (25A250A, Amplifier Research, USA) were used to activate a pair of slanted IDTs and to generate SAWs. For the acoustofluidic centrifuge system with dual spinning droplets, the microchannel was designed with a width of 200 μm and height of 100 μm.

Droplet generation and sample preparation

The micro droplets were generated using a pipette, and the nano droplets were generated using 1- and 0.5-μl microvolume liquid syringes (Scone Equine Group, AU). Ten-micrometer-, 5-μm-, 1-μm-, 970-nm-, 530-nm-, 100-nm-, 51-nm-, and 28-nm-diameter PS particles (Sigma-Aldrich, USA; Bangs Laboratories, USA) with different fluorescence tags are used in the experiments. Deoxyribonucleic acid chains from herring sperm in solution (Sigma-Aldrich, USA) were tested after staining with a SYTOX orange dye (Thermo Fisher Scientific, USA).

Small extracellular vesicle preparation procedure

The exosome sample was isolated from human plasma (Zen-Bio, USA) with a concentration of ~10^6/ml using differential ultracentrifugation. The general procedure is as follows:

1. Thaw plasma in a 37°C water bath until all the crystals of ice in the tubes have disappeared. After thawing is complete, mix the samples by gently vortexing for 10 s.
2. Centrifuge 45 ml of plasma at 3000*g* for 10 min at 8°C.
3. Dilute cleared plasma with PBS and spin at 10,000*g* for 30 min at 8°C. Resuspend and collect 10,000 pellets in 1.0 ml of PBS per tube.
4. Wash resuspended pellets using a 30-min spin at 10,000*g* at 8°C.
5. Spin supernatant at 103,745*g* for 4.5 hours at 8°C. Resuspend and collect 100,000 pellets in 0.5 ml of PBS per tube.
6. Combine resuspended plasma 100,000 pellets (2 ml in total), add 4 ml of PBS, and place on top of a three-part OptiPrep cushion (2 ml 50%/2 ml 30%/2 ml 10%). Centrifuge at 178,000*g* for 2 hours at 4°C. Collect 1 ml of the 30%/10% interface (ρ = 1.06 to 1.16 g/ml).
7. Dilute OptiPrep 30%/10% interface to 12 ml with PBS and spin at 120,000*g* for 2 hours at 8°C.
8. Resuspend pellets in 200 μl of PBS and analyze using NTA for confirmation.

Image acquisition and analysis

The microscope images and videos were acquired using an inverted microscope (TE2000-U, Nikon, Japan) equipped with a fast camera (Photron, Japan). The droplet spinning motion is captured with a frame rate of 3000 fps and analyzed using ImageJ [National Institutes of Health (NIH), MD, USA] and MATLAB R2016b (MathWorks, USA). The side view of the droplet spinning was captured using the Slow Mo mode of a cell phone with a frame rate of 240 fps. The postprocessed exosome sample was collected and visualized using TEM (FEI Tecnai G^2 Twin, FEI Company, USA) and a negative staining method. The nanoparticle size distribution and concentration pre- and postprocessing were analyzed using the Malvern Zetasizer (Malvern Instruments, UK) and NTA with a NanoSight LM10 apparatus (Amesbury, UK).

Numerical simulation of droplet spin and particle trajectory

Detailed numerical formulation, model description, force analysis, and parametric assessment can be found in the Supplementary Materials.

SUPPLEMENTARY MATERIALS

Supplementary material for this article is available at http://advances.sciencemag.org/cgi/content/full/7/1/eabc0467/DC1

REFERENCES AND NOTES

1. H. Lee, A. K. R. Lytton-Jean, Y. Chen, K. T. Love, A. I. Park, E. D. Karagiannis, A. Sehgal, W. Querbes, C. S. Zurenko, M. Jayaraman, C. G. Peng, K. Charisse, A. Borodovsky, M. Manoharan, J. S. Donahoe, J. Truelove, M. Nahrendorf, R. Langer, D. G. Anderson, Molecularly self-assembled nucleic acid nanoparticles for targeted *in vivo* siRNA delivery. *Nat. Nanotechnol.* **7**, 389–393 (2012).
2. C. M. H. Newman, T. Bettinger, Gene therapy progress and prospects: Ultrasound for gene transfer. *Gene Ther.* **14**, 465–475 (2007).
3. Y.-H. Lee, C.-A. Peng, Enhanced retroviral gene delivery in ultrasonic standing wave fields. *Gene Ther.* **12**, 625–633 (2005).
4. J. Sun, Y. Xianyu, X. Jiang, Point-of-care biochemical assays using gold nanoparticle-implemented microfluidics. *Chem. Soc. Rev.* **43**, 6239–6253 (2014).
5. X. Zhu, J. Wu, W. Shan, W. Tao, L. Zhao, J.-M. Lim, M. D'Ortenzio, R. Karnik, Y. Huang, J. Shi, O. C. Farokhzad, Polymeric nanoparticles amenable to simultaneous installation of exterior targeting and interior therapeutic proteins. *Angew. Chemie Int. Ed. Engl.* **55**, 3309–3312 (2016).
6. X. Huang, M. A. El-Sayed, Gold nanoparticles: Optical properties and implementations in cancer diagnosis and photothermal therapy. *J. Adv. Res.* **1**, 13–28 (2010).
7. K. Fan, C. Cao, Y. Pan, D. Lu, D. Yang, J. Feng, L. Song, M. Liang, X. Yan, Magnetoferritin nanoparticles for targeting and visualizing tumour tissues. *Nat. Nanotechnol.* **7**, 459–464 (2012).
8. M. A. Nash, J. N. Waitumbi, A. S. Hoffman, P. Yager, P. S. Stayton, Multiplexed enrichment and detection of malarial biomarkers using a stimuli-responsive iron oxide and gold nanoparticle reagent system. *ACS Nano* **6**, 6776–6785 (2012).
9. M. Stratakis, H. Garcia, Catalysis by supported gold nanoparticles: Beyond aerobic oxidative processes. *Chem. Rev.* **112**, 4469–4506 (2012).
10. G. Prieto, J. Zečević, H. Friedrich, K. P. de Jong, P. E. de Jongh, Towards stable catalysts by controlling collective properties of supported metal nanoparticles. *Nat. Mater.* **12**, 34–39 (2013).
11. H. Zhao, S. Sen, T. Udayabhaskararao, M. Sawczyk, K. Kučanda, D. Manna, P. K. Kundu, J.-W. Lee, P. Král, R. Klajn, Reversible trapping and reaction acceleration within dynamically self-assembling nanoflasks. *Nat. Nanotechnol.* **11**, 82–88 (2016).
12. A. Bekdemir, F. Stellacci, A centrifugation-based physicochemical characterization method for the interaction between proteins and nanoparticles. *Nat. Commun.* **7**, 13121 (2016).
13. S. Liu, T. D. Yuzvinsky, H. Schmidt, Effect of fabrication-dependent shape and composition of solid-state nanopores on single nanoparticle detection. *ACS Nano* **7**, 5621–5627 (2013).
14. J. Xu, K. J. Kwak, J. L. Lee, G. Agarwal, Lifting and sorting of charged Au nanoparticles by electrostatic forces in atomic force microscopy. *Small* **6**, 2105–2108 (2010).
15. A. Kunze, P. Tseng, C. Godzich, C. Murray, A. Caputo, F. E. Schweizer, D. Di Carlo, Engineering cortical neuron polarity with nanomagnets on a chip. *ACS Nano* **9**, 3664–3676 (2015).
16. A. H. J. Yang, S. D. Moore, B. S. Schmidt, M. Klug, M. Lipson, D. Erickson, Optical manipulation of nanoparticles and biomolecules in sub-wavelength slot waveguides. *Nature* **457**, 71–75 (2009).
17. B. J. Roxworthy, K. D. Ko, A. Kumar, K. H. Fung, E. K. C. Chow, G. L. Liu, N. X. Fang, K. C. Toussaint Jr., Application of plasmonic bowtie nanoantenna arrays for optical trapping, stacking, and sorting. *Nano Lett.* **12**, 796–801 (2012).
18. A. Ozcelik, J. Rufo, F. Guo, Y. Gu, P. Li, J. Lata, T. J. Huang, Acoustic tweezers for the life sciences. *Nat. Methods* **15**, 1021–1028 (2018).
19. K. Melde, A. G. Mark, T. Qiu, P. Fischer, Holograms for acoustics. *Nature* **537**, 518–522 (2016).
20. P. Li, Z. Mao, Z. Peng, L. Zhou, Y. Chen, P.-H. Huang, C. I. Truica, J. J. Drabick, W. S. El-Deiry, M. Dao, S. Suresh, T. J. Huang, Acoustic separation of circulating tumor cells. *Proc. Natl. Acad. Sci. U.S.A.* **112**, 4970–4975 (2015).
21. D. J. Collins, Z. Ma, Y. Ai, Highly localized acoustic streaming and size-selective submicrometer particle concentration using high frequency microscale focused acoustic fields. *Anal. Chem.* **88**, 5513–5522 (2016).
22. D. J. Collins, C. Devendran, Z. Ma, J. W. Ng, A. Neild, Y. Ai, Acoustic tweezers via sub–time-of-flight regime surface acoustic waves. *Sci. Adv.* **2**, ae1600089 (2016).
23. J. P. K. Armstrong, J. L. Puetzer, A. Serio, A. G. Guex, M. Kapnisi, A. Breant, Y. Zong, V. Assal, S. C. Skaalure, O. King, T. Murty, C. Meinert, A. C. Franklin, P. G. Bassindale, M. K. Nichols, C. M. Terracciano, D. W. Hutmacher, B. W. Drinkwater, T. J. Klein, A. W. Perriman, M. M. Stevens, Engineering anisotropic muscle tissue using acoustic cell patterning. *Adv. Mater.* **30**, 1802649 (2018).
24. M. V. Patel, A. R. Tovar, A. P. Lee, Lateral cavity acoustic transducer as an on-chip cell/particle microfluidic switch. *Lab Chip* **12**, 139–145 (2012).
25. R. Barnkob, P. Augustsson, T. Laurell, H. Bruus, Acoustic radiation-and streaming-induced microparticle velocities determined by microparticle image velocimetry in an ultrasound symmetry plane. *Phys. Rev. E.* **86**, 56307 (2012).
26. H. Li, J. R. Friend, L. Y. Yeo, Surface acoustic wave concentration of particle and bioparticle suspensions. *Biomed. Microdevices* **9**, 647–656 (2007).
27. M. Wu, Z. Mao, K. Chen, H. Bachman, Y. Chen, J. Rufo, L. Ren, P. Li, L. Wang, T. J. Huang, Acoustic separation of nanoparticles in continuous flow. *Adv. Funct. Mater.* **27**, 1606039 (2017).

28. M. S. Limaye, J. J. Hawkes, W. T. Coakley, Ultrasonic standing wave removal of microorganisms from suspension in small batch systems. *J. Microbiol. Methods* **27**, 211–220 (1996).
29. B. Hammarström, T. Laurell, J. Nilsson, Seed particle-enabled acoustic trapping of bacteria and nanoparticles in continuous flow systems. *Lab Chip* **12**, 4296–4304 (2012).
30. M. Antfolk, P. B. Muller, P. Augustsson, H. Bruus, T. Laurell, Focusing of sub-micrometer particles and bacteria enabled by two-dimensional acoustophoresis. *Lab Chip* **14**, 2791–2799 (2014).
31. Z. Mao, P. Li, M. Wu, H. Bachman, N. Mesyngier, X. Guo, S. Liu, F. Costanzo, T. J. Huang, Enriching nanoparticles *via* acoustofluidics. *ACS Nano* **11**, 603–612 (2017).
32. D. J. Collins, Z. Ma, J. Han, Y. Ai, Continuous micro-vortex-based nanoparticle manipulation *via* focused surface acoustic waves. *Lab Chip* **17**, 91–103 (2017).
33. N. Ashgriz, *Handbook of Atomization and Sprays: Theory and Applications* (Springer Science & Business Media, 2011).
34. R. J. A. Hill, L. Eaves, Nonaxisymmetric shapes of a magnetically levitated and spinning water droplet. *Phys. Rev. Lett.* **101**, 234501 (2008).
35. C. L. Shen, W. J. Xie, B. Wei, Parametrically excited sectorial oscillation of liquid drops floating in ultrasound. *Phys. Rev. E* **81**, 046305 (2010).
36. G. Destgeer, H. Cho, B. H. Ha, J. H. Jung, J. Park, H. J. Sung, Acoustofluidic particle manipulation inside a sessile droplet: Four distinct regimes of particle concentration. *Lab Chip* **16**, 660–667 (2016).
37. Y. Bourquin, A. Syed, J. Reboud, L. C. Ranford-Cartwright, M. P. Barrett, J. M. Cooper, Rare-cell enrichment by a rapid, label-free, ultrasonic isopycnic technique for medical diagnostics. *Angew. Chem. Int. Ed. Engl.* **53**, 5587–5590 (2014).
38. P. R. Rogers, J. R. Friend, L. Y. Yeo, Exploitation of surface acoustic waves to drive size-dependent microparticle concentration within a droplet. *Lab Chip* **10**, 2979–2985 (2010).
39. R. Shilton, M. K. Tan, L. Y. Yeo, J. R. Friend, Particle concentration and mixing in microdrops driven by focused surface acoustic waves. *J. Appl. Phys.* **104**, 014910 (2008).
40. W. Thielicke, E. J. Stamhuis, PIVlab-time-resolved digital particle image velocimetry tool for MATLAB (version: 1.35). *J. Open Res. Softw.* **2**, 10.6084/m9.figshare.1092508 (2014).
41. W. Thielicke, E. J. Stamhuis, PIVlab–towards user-friendly, affordable and accurate digital particle image velocimetry in MATLAB. *J. Open Res. Softw.* **2**, e30 (2014).
42. M. Yáñez-Mó, P. R.-M. Siljander, Z. Andreu, A. B. Zavec, F. E. Borràs, E. I. Buzas, K. Buzas, E. Casal, F. Cappello, J. Carvalho, E. Colás, A. C.-d. Silva, S. Fais, J. M. Falcon-Perez, I. M. Ghobrial, B. Giebel, M. Gimona, M. Graner, I. Gursel, M. Gursel, N. H. H. Heegaard, A. Hendrix, P. Kierulf, K. Kokubun, M. Kosanovic, V. Kralj-Iglic, E.-M. Krämer-Albers, S. Laitinen, C. Lässer, T. Lener, E. Ligeti, A. Linē, G. Lipps, A. Llorente, J. Lötvall, M. Manček-Keber, A. Marcilla, M. Mittelbrunn, I. Nazarenko, E. N. M. N.-'t. Hoen, T. A. Nyman, L. O'Driscoll, M. Olivan, C. Oliveira, É. Pállinger, H. A. Del Portillo, J. Reventós, M. Rigau, E. Rohde, M. Sammar, F. Sánchez-Madrid, N. Santarém, K. Schallmoser, M. S. Ostenfeld, W. Stoorvogel, R. Stukelj, S. G. Van der Grein, M. H. Vasconcelos, M. H. M. Wauben, O. De Wever, Biological properties of extracellular vesicles and their physiological functions. *J. Extracell. vesicles.* **4**, 27066 (2015).
43. P. Zhang, X. Zhou, M. He, Y. Shang, A. L. Tetlow, A. K. Godwin, Y. Zeng, Ultrasensitive detection of circulating exosomes with a 3D-nanopatterned microfluidic chip. *Nat. Biomed. Eng.* **3**, 438–451 (2019).
44. H. Zhang, D. Freitas, H. S. Kim, K. Fabijanic, Z. Li, H. Chen, M. T. Mark, H. Molina, A. B. Martin, L. Bojmar, J. Fang, S. Rampersaud, A. Hoshino, I. Matei, C. M. Kenific, M. Nakajima, A. P. Mutvei, P. Sansone, W. Buehring, H. Wang, J. P. Jimenez, L. Cohen-Gould, N. Paknejad, M. Brendel, K. Manova-Todorova, A. Magalhães, J. A. Ferreira, H. Osório, A. M. Silva, A. Massey, J. R. Cubillos-Ruiz, G. Galletti, P. Giannakakou, A. M. Cuervo, J. Blenis, R. Schwartz, M. S. Brady, H. Peinado, J. Bromberg, H. Matsui, C. A. Reis, D. Lyden, Identification of distinct nanoparticles and subsets of extracellular vesicles by asymmetric flow field-flow fractionation. *Nat. Cell Biol.* **20**, 332–343 (2018).
45. B. H. Wunsch, J. T. Smith, S. M. Gifford, C. Wang, M. Brink, R. L. Bruce, R. H. Austin, G. Stolovitzky, Y. Astier, Nanoscale lateral displacement arrays for the separation of exosomes and colloids down to 20 nm. *Nat. Nanotechnol.* **11**, 936–940 (2016).
46. A. Cheruvanky, H. Zhou, T. Pisitkun, J. B. Kopp, M. A. Knepper, P. S. T. Yuen, R. A. Star, Rapid isolation of urinary exosomal biomarkers using a nanomembrane ultrafiltration concentrator. *Am. J. Physiol. Physiol.* **292**, F1657–F1661 (2007).
47. N. Francois, H. Xia, H. Punzmann, P. W. Fontana, M. Shats, Wave-based liquid-interface metamaterials. *Nat. Commun.* **8**, 14325 (2017).
48. M. Wu, A. Ozcelik, J. Rufo, Z. Wang, R. Fang, T. J. Huang, Acoustofluidic separation of cells and particles. *Microsyst. Nanoeng.* **5**, 32 (2019).
49. T. Salafi, K. K. Zeming, Y. Zhang, Advancements in microfluidics for nanoparticle separation. *Lab Chip* **17**, 11–33 (2017).
50. S. B. Berry, J. J. Lee, J. Berthier, E. Berthier, A. B. Theberge, Open channel droplet-based microfluidics. *bioRxiv* , 436675 (2018).
51. M. Karimi, G. Akdogan, K. H. Dellimore, S. M. Bradshaw, Comparison of different drag coefficient correlations in the CFD modelling of a laboratory-scale Rushton-turbine flotation tank, Proceedings of the Ninth International Conference on CFD in the Minerals and Process Industries, Melbourne, Australia, 10-12 December 2012.
52. F. Yilmaz, M. Y. Gundogdu, Analysis of conventional drag and lift models for multiphase CFD modeling of blood flow. *Korea Aust. Rheol. J.* **21**, 161–173 (2009).
53. J. Lighthill, Acoustic streaming. *J. Sound Vib.* **61**, 391–418 (1978).
54. M. Alghane, B. X. Chen, Y. Q. Fu, Y. Li, J. K. Luo, A. J. Walton, Experimental and numerical investigation of acoustic streaming excited by using a surface acoustic wave device on a 128° YX-$LiNbO_3$ substrate. *J. Micromech. Microeng.* **21**, 15005 (2011).
55. A. B. COMSOL, Comsol multiphysics® v.5.4 www.comsol.com. Stockholm, Sweden. COMSOL AB (2018).
56. J. M. Martel, M. Toner, Inertial focusing in microfluidics. *Annu. Rev. Biomed. Eng.* **16**, 371–396 (2014).
57. L. P. Gor'Kov, On the forces acting on a small particle in an acoustical field in an ideal fluid. *Sov. Phys. Dokl.* **6**, 773 (1962).
58. A. Bobrie, M. Colombo, S. Krumeich, G. Raposo, C. Théry, Diverse subpopulations of vesicles secreted by different intracellular mechanisms are present in exosome preparations obtained by differential ultracentrifugation. *J. Extracell. vesicles.* **1**, 18397 (2012).
59. R. J. Lobb, M. Becker, S. Wen Wen, C. S. F. Wong, A. P. Wiegmans, A. Leimgruber, A. Möller, Optimized exosome isolation protocol for cell culture supernatant and human plasma. *J. Extracell. vesicles.* **4**, 27031 (2015).
60. D. W. Greening, R. Xu, H. Ji, B. J. Tauro, R. J. Simpson, in *Proteomic Profiling* (Springer, 2015), pp. 179–209.
61. H. Shin, C. Han, J. M. Labuz, J. Kim, J. Kim, S. Cho, Y. S. Gho, S. Takayama, J. Park, High-yield isolation of extracellular vesicles using aqueous two-phase system. *Sci. Rep.* **5**, 13103 (2015).
62. S. Mathivanan, J. W. E. Lim, B. J. Tauro, H. Ji, R. L. Moritz, R. J. Simpson, Proteomics analysis of A33 immunoaffinity-purified exosomes released from the human colon tumor cell line LIM1215 reveals a tissue-specific protein signature. *Mol. Cell. Proteomics* **9**, 197–208 (2010).
63. H. Qi, C. Liu, L. Long, Y. Ren, S. Zhang, X. Chang, X. Qian, H. Jia, J. Zhao, J. Sun, X. Hou, X. Yuan, C. Kang, Blood exosomes endowed with magnetic and targeting properties for cancer therapy. *ACS Nano* **10**, 3323–3333 (2016).
64. Z. Zhao, Y. Yang, Y. Zeng, M. He, A microfluidic ExoSearch chip for multiplexed exosome detection towards blood-based ovarian cancer diagnosis. *Lab Chip* **16**, 489–496 (2016).
65. S. S. Kanwar, C. J. Dunlay, D. M. Simeone, S. Nagrath, Microfluidic device (ExoChip) for on-chip isolation, quantification and characterization of circulating exosomes. *Lab Chip* **14**, 1891–1900 (2014).

Acknowledgments

Funding: We acknowledge support from the NIH (UG3TR002978, R01GM132603, R01GM135486, R33CA223908, R01GM127714, and R01HD086325), the United States Army Medical Research Acquisition Activity (W81XWH-18-1-0242), and the NSF (ECCS-1807601). **Author contributions:** Y.G., C.C., and Z.M. developed the system concept. Y.G. led the experimental work. Y.G., C.C., and Z.M. led the theoretical and numerical analyses. Z.W. and Y.O. contributed to biosample preparation and process. P.Z., J.Z., S.Y., J.R., and S.Z. contributed to the device fabrication and improvement. D.T.W.W., Y.S., and T.J.H. provided guidance and contributed to the design and analysis throughout the project. Y.G., C.C., H.B., R.B., Z.M., J.M., J.R., P.Z., Y.O., Y.S., D.T.W.W., and T.J.H. cowrote the manuscript. **Competing interests:** T.J.H. has four U.S. patents (patent numbers: 8,573,060; 9,608,547; 9,606,086; and 9,757,699) related to acoustofluidics and acoustic tweezers. T.J.H. has also cofounded a startup company, Ascent Bio-Nano Technologies Inc., to commercialize technologies involving acoustofluidics and acoustic tweezers. D.T.W.W. has equity in Liquid Diagnostics and consultant to Mars-Wrigley and Colgate Palmolive. All other authors declare that they have no competing interests. **Data and materials availability:** All data needed to evaluate the conclusions in the paper are present in the paper and/or the Supplementary Materials. Further information is available from the corresponding author upon reasonable request.

Submitted 3 April 2020
Accepted 5 November 2020
Published 1 January 2021
10.1126/sciadv.abc0467

Citation: Y. Gu, C. Chen, Z. Mao, H. Bachman, R. Becker, J. Rufo, Z. Wang, P. Zhang, J. Mai, S. Yang, J. Zhang, S. Zhao, Y. Ouyang, D. T. W. Wong, Y. Sadovsky, T. J. Huang, Acoustofluidic centrifuge for nanoparticle enrichment and separation. *Sci. Adv.* **7**, eabc0467 (2021).